

This is the accepted manuscript made available via CHORUS. The article has been published as:

Search for multipolar instability in $\text{URu}_{\{2\}}\text{Si}_{\{2\}}$ studied by ultrasonic measurements under pulsed magnetic field

T. Yanagisawa, S. Mombetsu, H. Hidaka, H. Amitsuka, P. T. Cong, S. Yasin, S. Zherlitsyn, J. Wosnitza, K. Huang, N. Kanchanavatee, M. Janoschek, M. B. Maple, and D. Aoki

Phys. Rev. B **97**, 155137 — Published 17 April 2018

DOI: [10.1103/PhysRevB.97.155137](https://doi.org/10.1103/PhysRevB.97.155137)

Search for Multipolar Instability in URu₂Si₂ Studied by Ultrasonic Measurements under Pulsed Magnetic Field

T. Yanagisawa,^{1,*} S. Mombetsu,¹ H. Hidaka,¹ H. Amitsuka,¹ P. T. Cong,² S. Yasin,² S. Zherlitsyn,²
J. Wosnitza,^{3,2} K. Huang,⁴ N. Kanchanavatee,⁴ M. Janoschek,^{4,5} M. B. Maple,⁴ and D. Aoki^{6,7}

¹*Department of Physics, Hokkaido University, Sapporo 060-0810, Japan*

²*Hochfeld-Magnetlabor Dresden (HLD-EMFL), Helmholtz-Zentrum Dresden-Rossendorf, 01328 Dresden, Germany*

³*Institut für Festkörperphysik und Materialphysik, TU Dresden, 01062 Dresden, Germany*

⁴*Department of Physics, University of California, San Diego, La Jolla, California 92093, USA*

⁵*LosAlamos National Laboratory, LosAlamos, NM 87545, USA*

⁶*IMR, Tohoku University, Oarai, Ibaraki 311-1313, Japan*

⁷*INAC/PHELIQS, CEA-Grenoble, 38054 Grenoble, France*

(Dated: April 3, 2018)

The elastic properties of URu₂Si₂ in the high-magnetic field region above 40 T, over a wide temperature range from 1.5 to 120 K, were systematically investigated by means of high-frequency ultrasonic measurements. The investigation was performed at high magnetic fields to better investigate the innate bare 5*f*-electron properties, since the unidentified electronic thermodynamic phase of unknown origin, so called ‘hidden order’ (HO) and associated hybridization of conduction and *f*-electron (*c-f* hybridization) are suppressed at high magnetic fields. From the three different transverse modes we find contrasting results; both the $\Gamma_4(B_{2g})$ and $\Gamma_5(E_g)$ symmetry modes C_{66} and C_{44} show elastic softening that is enhanced above 30 T, while the characteristic softening of the $\Gamma_3(B_{1g})$ symmetry mode $(C_{11} - C_{12})/2$ is suppressed in high magnetic fields. These results underscore the presence of a hybridization-driven $\Gamma_3(B_{1g})$ lattice instability in URu₂Si₂. However, the results from this work cannot be explained by using existing crystalline-electric field (CEF) schemes applied to the quadrupolar susceptibility in a local 5*f*² configuration. Instead, we present an analysis based on a band Jahn-Teller effect.

I. INTRODUCTION

The heavy-fermion unconventional superconductor URu₂Si₂ undergoes an enigmatic phase transition at $T_O = 17.5$ K to the so called ‘hidden order (HO)’ phase^{1–3}, whose order parameter still remains unsolved⁴. This compound has a body-centered-tetragonal (bct) ThCr₂Si₂-type crystal structure (space group No. 139, $I4/mmm$; D_{4h}^{17}). Recently, several experimental findings regarding a possible symmetry lowering of the electron and/or lattice system in the HO phase have been reported; including results of magnetic torque⁵, synchrotron x-ray⁶, Raman scattering⁷, and elastoresistance measurements⁸. However, the proposed broken symmetries conflict with each other. Many theories have been proposed to explain the HO phase; e.g., higher multipolar order from rank 3 to 5^{9–13}, hastatic order¹⁴, spin inter-orbital density wave¹⁵, and dynamic antiferromagnetic moment fluctuations.¹⁶ There is no comprehensive interpretation, which can explain all of the experimental observations.

With high magnetic fields applied along the [001] axis at low temperatures, URu₂Si₂ undergoes three metamagnetic transitions in the range between 35 and 39 T which are followed by a collapse of the HO phase¹⁷. In Fig. 1(b), we show a temperature-magnetic-field phase diagram of URu₂Si₂ for $H \parallel [001]$, which is constructed from the data of the present work and previous magnetization measurements¹⁸. First, the HO phase is suppressed at 35 T, followed by a cascade of transitions, where the spin-density wave with a propagation wave

vector $\mathbf{k} = (0.6, 0, 0)$ is established in the intermediate phase¹⁹. Finally, the system enters the polarized paramagnetic (PPM) regime in the high-magnetic-field region above 40 T¹⁷. URu₂Si₂ also exhibits a strong hybridization between conduction and 5*f* electrons (*c-f* hybridization) below $T^* \sim 50$ K in low magnetic fields. This *c-f* hybridization is also suppressed in association with the collapse of HO under high magnetic fields above 40 T for $H \parallel [001]$ ¹⁸. Beyond 40 T, the electronic ground state of URu₂Si₂ changes from delocalized to a more localized 5*f*-electron regime¹⁸. Understanding the dual nature of the uranium 5*f* electron that are neither fully localized nor itinerant will likely provide insight in the origin of the HO. No theory has been developed which fully describes both the hybridization effect and the localized electron degrees of freedom. There are two approaches to overcome these issues; either starting from the itinerant electron system (strong-coupling limit) or from the localized electron system (weak-coupling limit). A constraint is that the ‘symmetry’ of the order parameter itself must be the same, both in the itinerant and localized components of the 5*f*-electrons as they both play a role in developing the HO. Ultrasonic measurement is one of the sensitive probing techniques to investigate both itinerant band instabilities, such as the band-Jahn Teller effect, and the local anisotropic charge distribution, such as that found in multipolar ordering. Therefore the present work is aimed at obtaining better information on the dual nature of the 5*f*-electron states in URu₂Si₂. Our recent investigation of the elastic constant $(C_{11} - C_{12})/2$ of URu₂Si₂ under pulsed-magnetic fields strongly sug-

gests that the hybridized electronic state possesses an orthorhombic ($x^2 - y^2$) lattice instability with $\Gamma_3(B_{1g})$ symmetry²⁰. The origin of the lattice instability is considered to be either a potential deformation due to the Jahn-Teller effect of hybridized bands or a simple CEF effect of uranium's 5*f* electrons; however, the origin of the $\Gamma_3(B_{1g})$ lattice instability and its relation to the HO parameter are still open questions. In order to verify that the system does not exhibit a lattice instability for other symmetries, and to examine the theoretical predictions of CEF ground-state schemes for the high magnetic fields and related higher-multipolar order parameter scenarios for the HO phase as well, we study elastic responses of the other symmetry-breaking strains. In the present work, we report on the responses of C_{44} with $\Gamma_5(E_g)$ symmetry and C_{66} with $\Gamma_4(B_{2g})$ symmetry under high magnetic field, and compare these results with the previously reported $(C_{11} - C_{12})/2$ with $\Gamma_3(B_{1g})$ symmetry.

II. EXPERIMENTAL DETAILS

We investigated two single crystals of URu₂Si₂ grown using the Czochralski technique by a tetra-arc furnace at UC San Diego (sample #1) and CEA Grenoble (sample #2). For sample #1, the dimensions are $3.8 \times 1.8 \times 1.2$ mm³ with parallel [110] facets as grown. Residual resistivity ratio (RRR) ~ 10 was used for $(C_{11} - C_{12})/2$, C_{44} , and C_{33} measurements. For sample #2, $3.38 \times 1.67 \times 1.5$ mm³ with parallel [100] facets, annealed in vacuum, RRR ~ 29 is used for C_{11} , C_{44} , C_{66} . Note, there is no obvious sample dependence in the magnetic field dependence of C_{44} for both samples, except for a difference in the signal-to-noise ratio. The sample surfaces were well polished and characterized by x-ray Laue diffraction to check the characteristic symmetries of the facets. Ultrasound was generated and detected by using LiNbO₃ transducers with a thickness of 40-100 μ m, which were fixed on the sample surfaces with RTV silicone or superglue. We used pulsed magnetic fields up to 68 T with pulse duration of about 150 ms at the Dresden High Magnetic Field Laboratory. The sound-velocity measurements were performed by using a conventional phase comparative method using a digital storage oscilloscope. Ultrasound induces both linear strain and a rotation field (similar to Raman modes). A summary with D_{4h} point group are shown in Table I) in the solid, which behave as conjugate fields for the electric quadrupole or electric hexadecapole moments. These multipolar responses can be observed as a sound-velocity change and ultrasonic attenuation via electron-phonon interaction. The sound velocity v_{ij} is converted to the elastic constant C_{ij} by using the formula; $C_{ij} = \rho v_{ij}^2$. Here, $\rho = 10.01$ (g/cm³) is the density of URu₂Si₂.

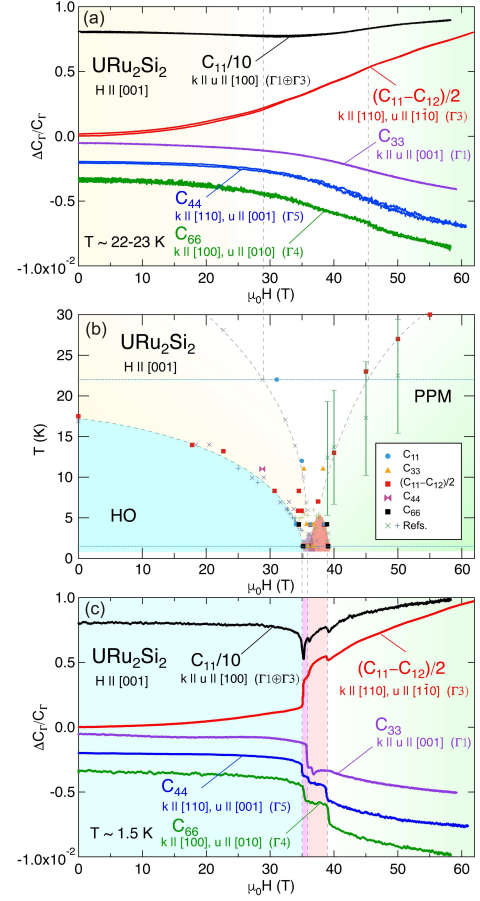


FIG. 1. (a) Magnetic field dependence of elastic constants C_{11} , $(C_{11} - C_{12})/2$, C_{33} , C_{44} , and C_{66} at fixed temperatures of 22-23 K for $H \parallel [001]$. C_{11} is divided by 10 to allow a better comparison. (b) The temperature-magnetic-field phase diagram of URu₂Si₂ for $H \parallel [001]$ is compiled from the present ultrasonic experiments and the previous results¹⁸. The blue horizontal lines indicate the trajectories where the pulsed-field measurements were performed at fixed temperature of 22.5 and 1.5 K. Part (c) is the same as (a) at 1.5 K. The dotted lines are visual aids.

III. RESULTS

In Fig. 1, we show the magnetic-field dependence of the following elastic constants $C_{11}/10$, $(C_{11} - C_{12})/2$, C_{33} , C_{44} , and C_{66} at fixed temperatures of (a) 22-23 K and (c) 1.5 K for $H \parallel [001]$ which are measured with ultrasonic frequencies of 75 MHz for C_{11} , 159.5 MHz for $(C_{11} - C_{12})/2$, 78.7 MHz for C_{33} , 164 MHz for C_{44} , and 166 MHz for C_{66} . At 22-23 K, the elastic constants C_{33} , C_{44} , and C_{66} decrease with increasing magnetic-field through the cross-over region of the *c-f* hybridization (below 30 T) and toward the polar-paramagnetic region (above 45 T), while C_{11} and $(C_{11} - C_{12})/2$, both related to the Γ_3 -symmetry response, increase above 35 T.

The magnetic field-temperature (H - T) phase diagram is displayed in Fig. 1(b) for comparison, where the hor-

TABLE I. Symmetry, symmetrized strain and rotation, and multipole for different elastic constants.

Symmetry (D_{4h} group)	Strain and Rotation	Multipole	Elastic Constant
$\Gamma_1(A_{1g})$	$\epsilon_{xx}, \epsilon_{yy}$	-	$C_{33} = -3C_B + 4C_u + 4C_{13}$
$\Gamma_1 \oplus \Gamma_3(A_{1g} \oplus B_{1g})$	$\epsilon_{zz} = \epsilon_B/3 - \epsilon_B/\sqrt{3}$	-	$C_{11} = 3C_B - C_u + (C_{11} - C_{12})/2 - 2C_{13}$
$\Gamma_3(B_{1g})$	$\epsilon_v = \epsilon_{xx} - \epsilon_{yy}$	$O_v = \sqrt{3}(J_x^2 - J_y^2)/2$	$C_v = (C_{11} - C_{12})/2$
$\Gamma_4(B_{2g})$	ϵ_{xy}	$O_{xy} = \sqrt{3}(J_x J_y - J_y J_x)/2$	C_{66}
$\Gamma_5(E_g)$	ϵ_{yz}	$O_{yz} = \sqrt{3}(J_y J_z - J_z J_y)/2$	C_{44}
	ϵ_{zx}	$O_{zx} = \sqrt{3}(J_z J_x - J_x J_z)/2$	C_{44}
$\Gamma_1(A_{1g})$	$\epsilon_B = \epsilon_{xx} + \epsilon_{yy} + \epsilon_{zz}$	-	$C_B = (2C_{11} + 2C_{12} + 4C_{13} + C_{33})/9$
$\Gamma_1(A_{1g})$	$\epsilon_u = (2\epsilon_{zz} - \epsilon_{xx} - \epsilon_{yy})$	$O_u = \sqrt{3}(2J_z^2 - J_x^2 - J_y^2)/2$	$C_u = (C_{11} + C_{12} - 4C_{13} + 2C_{33})/6$
$\Gamma_2(A_{2g})$	ω_{xy}	$H_z^\alpha = \sqrt{35}(J_+^4 - J_-^4)/4i$	C_{66}, C_v

izontal lines connect to features in the elastic constant data. In Fig. 1(c), all elastic constants at 1.5 K show successive step-like anomalies through the cascade of metamagnetic transitions with the destruction of the hidden order²¹. The overall tendency to decrease or increase with field reproduces from the magnetic-field dependence at 22-23 K [Fig. 1(a)]. Such a clear contrast of decreasing or increasing tendency in the three transverse modes in the paramagnetic phase just above $T_O \sim 17.5$ K supports the idea that the Γ_3 -type orthorhombic lattice instability is related to a symmetry-breaking band instability that arises due to the c - f hybridization and is probably linked to the origin of HO in this compound²⁰.

One may consider the possibility of the magnetostriction on the sound-velocity change, since the magnetic field change of the elastic constant looks very similar to the magnetization and magnetostriction change in pulsed-magnetic fields. However, by applying magnetic field along the [001] axis of URu_2Si_2 , the c -axis length decreases only by $\Delta L_c/L_c \sim 10^{-4}$ at 45 T and 1.5 K, and the a axis expands by the same order of magnitude due to the Poisson effect²². In the present case, such an effect would mainly lead to enhance softening of the longitudinal C_{11} mode in the vicinity of the cascade transitions. C_{11} includes a contribution from the bulk modulus (volume strain). Based on the modified Ehrenfest equation²³, the estimated contribution of the magnetostriction to the sound-velocity change is $\Delta v_{ij}/v_{ij} \sim 10^{-4}$, which is less than only 5% of the total velocity change $\sim 2 \times 10^{-3}$ of the transverse ultrasonic modes C_{44} , C_{66} , and $(C_{11} - C_{12})/2$. The hardening of $(C_{11} - C_{12})/2$ at the collapse of the HO phase has a tendency opposite to the magnetostriction along [100], since it is equivalent to $1/\sqrt{2}$ of the magnetostriction along [110]. Consequently, Γ_3 elastic response originates from the drastic change of the transverse acoustic phonon dispersion due to strong coupling to the $5f$ -electrons.

In Figs. 2 (d) and (g), we show the isotherms of the modes C_{44} and C_{66} as a function of increasing and decreasing magnetic field applied along [001]. For comparison, our previous results²⁰ for the $(C_{11} - C_{12})/2$ are also shown in Fig. 2 (a). From these data, we determined the

elastic constants as a function of temperature in fixed magnetic field, shown in Figs. 2 (c), (f), and (i). The middle column combines 3-dimensional plots of the elastic constants vs. temperature and magnetic field $H \parallel c$ for the three different symmetries; (b) $(C_{11} - C_{12})/2$ for the $\Gamma_3(B_{1g})$, (e) C_{66} for the $\Gamma_5(E_g)$, and (h) C_{44} for the $\Gamma_4(B_{2g})$ of the D_{4h} point group symmetry. The bottom of each cubic box shows the $H - T$ phase diagram. The blue-white-red color gradation indicates the relative stiffness of each ultrasonic mode, stiffer in blue and softer in red. In the soft-mode regions, the system may indicate lattice instabilities of the corresponding symmetry. For example, for the $(C_{11} - C_{12})/2$ mode, the corresponding $\Gamma_3(B_{1g})$ lattice instability is enhanced in the low-temperature and low-magnetic-field region, where strong c - f hybridization occurs, and suppressed at high temperatures and high magnetic fields. The $\Gamma_4(B_{2g})$ and $\Gamma_5(E_g)$ modes show the opposite tendency. Such a clear difference in the three transverse modes indicates the presence of the $\Gamma_3(B_{1g})$ lattice instability in the HO phase, and in the strong c - f hybridization region at low-magnetic fields in URu_2Si_2 .

IV. DISCUSSION

A. Band Jahn-Teller Model: (Delocalized $5f$ -electron state)

In Figs. 3 (a), (b), and (c) the normalized elastic constants vs. temperature at various magnetic fields are shown for (a) $\Gamma_3(B_{1g})$: $(C_{11} - C_{12})/2$, (b) $\Gamma_4(B_{2g})$: C_{66} , and (c) $\Gamma_5(E_g)$: C_{44} , with the phonon background subtracted. For simplicity, we made phenomenological fits to the elastic constants of $ThRu_2Si_2$ measured from 300 K to 1.5 K in zero magnetic field as the phonon background shown as the dotted lines in Figs. 2(c), (f), and (i). A similar subtraction was also performed in our previous work.²⁴ First, we analyzed the softening of $(C_{11} - C_{12})/2$ by using the phenomenological theory of the band-Jahn-Teller (BJT) effect assuming a rigid degenerate two-band state²⁵. The solid lines in Fig. 3(a) were calculated from

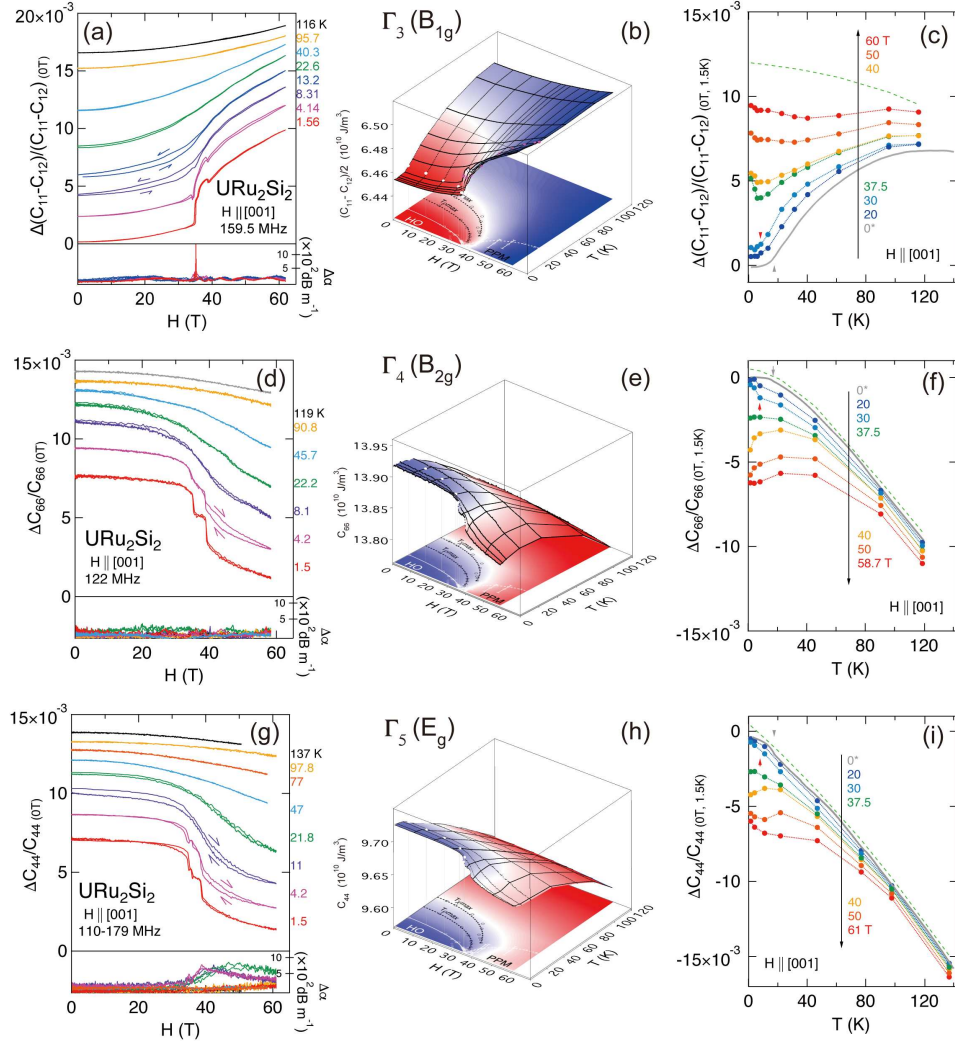


FIG. 2. Left column: Magnetic-field dependence of the elastic constants (a) $(C_{11} - C_{12})/2$, (d) C_{66} , and (g) C_{44} for $H \parallel [001]$ of URu_2Si_2 at selected temperatures. The lower panel in each figure shows the sound-attenuation change $\Delta\alpha$ vs. H . These data was taken for both increasing and decreasing field. Middle column: Three-dimensional plots of the elastic constants vs. temperature and magnetic field aligned along the c axis of URu_2Si_2 . The bottom of the boxes shows the magnetic field-temperature phase diagram of URu_2Si_2 for $H \parallel [001]$. Right column: Normalized elastic constants vs. temperature at various magnetic fields $H \parallel [001]$ converted from (a), (d), and (g), except for the zero-magnetic field data. Green dotted lines indicate the estimated phonon background. The panels arranged horizontally show the modes, (a), (b), (c) for $(C_{11} - C_{12})/2$ reprinted from Ref. [20], (d), (e), (f) for C_{66} ; and (g), (h), (i) for C_{44} .

the following equation:

$$\frac{(C_{11} - C_{12})}{2} = C_{\text{ph}} - 2d^2 N_0 \{1 - e^{-(E_F - E_0)/k_B T}\}. \quad (1)$$

Here, C_{ph} is the phonon background [as shown in Fig. 2(c)], d is a deformation-potential coupling constant, N_0 is the density of states at the Fermi energy E_F , and E_0 is the energy at the bottom of the conduction band. The term $2d^2 N_0$ is set to be temperature independent. Figure 4 shows the magnetic-field dependence of the fit parameters ($2d^2 N_0$) and $(E_F - E_0)$. We obtain $E_F - E_0 = 43$ K at 0 T and $E_F - E_0 = 28$ K at 35 T. The value of $2d^2 N_0 = 0.071 \times 10^{10} \text{ J m}^{-3}$ at 0 T gradually decreases with increasing magnetic field, which is consistent with

the reduction of c - f hybridization under magnetic field, where causes a weakening of the deformation-potential coupling. The parameters obtained below 30 T are comparable to the values reported for the typical band-Jahn-Teller system $\text{LaAg}_{1-x}\text{In}_x$ ²⁶, where the compounds with $x = 0$ and $x = 0.11$ do not show structural transition but exhibit a softening in $(C_{11} - C_{12})/2$ due to Γ_3 lattice instability. Here for URu_2Si_2 , the obtained deformation-potential coupling energy is less than 1/5 of the value of LaAg ($x = 0$, $2d^2 N_0 = 0.375 \times 10^{10} \text{ J m}^{-3}$), suggesting that the effect is too weak to induce a structural phase transition. Above 40 T, the gap and the fitting error bar drastically increase, which appears to be extrinsic and shows the limitations of this theory.

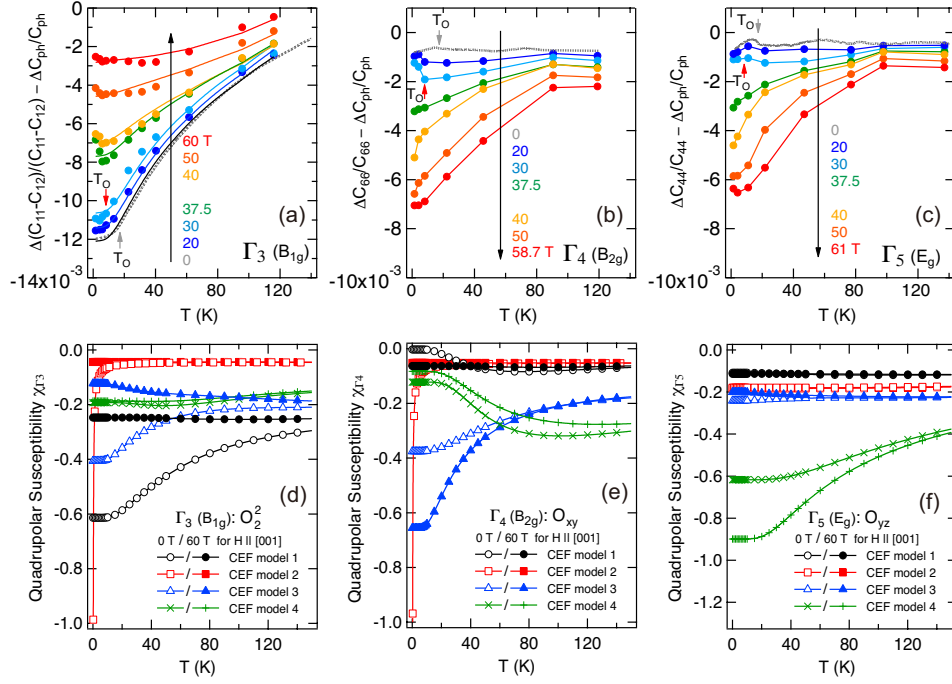


FIG. 3. Temperature dependence of the normalized elastic constants of (a) Γ_3 : $(C_{11} - C_{12})/2$, (b) Γ_4 : C_{66} , and (c) Γ_5 : C_{44} at various magnetic fields $H \parallel [001]$, where the phonon background is subtracted. Solid lines in (a) are calculated by using the band-Jahn-Teller model (see text), and the solid lines in (b) and (c) are visual aids. Calculated uniform quadrupolar susceptibilities of (d) Γ_3 : O_2^2 , (e) Γ_4 : O_{xy} and (f) Γ_5 : O_{yz} for different CEF schemes (see Table II) at 0 and 60 T.

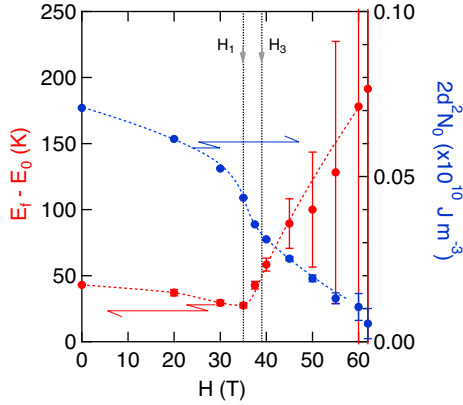


FIG. 4. Magnetic field dependence of the BJT fit parameters for $(C_{11} - C_{12})/2$: The gap between the two levels $E_\Gamma - E_0$ (red, left axis) and $2d^2N_0$ (blue, right axis, see text for details). The dotted curves a visual aid.

B. Crystalline Electric Field Models: (Localized $5f$ -electron state)

We compare elastic responses obtained in the high-magnetic field region with uniform quadrupolar susceptibilities, which are calculated by using CEF schemes in the $5f^2$ configuration, proposed thus far. We have considered a variety of CEF level schemes, especially based on the $U^{4+}(5f^2)$ ionization and non-Kramers 3H_4 ($J=4$)

Hund's rule ground-state multiplet; a non-Kramers configuration can easily reproduce the reported anisotropic magnetization along the a and c axis of this compound²⁷. The details of the four CEF schemes considered are listed in Table II. It should be noted that the present CEF scheme 1 has two lowest-lying $U-5f$ singlets; $\Gamma_1^{(1)} = \alpha(|4\rangle + |-4\rangle) - \beta|0\rangle$ and $\Gamma_2 = i(|4\rangle - |-4\rangle)/\sqrt{2}$, which is identical to the level scheme in the theoretical models originally predicting the A_{2g} -type hexadecapolar order as the order parameter of the HO state, which have been proposed by Haule and Kotliar¹⁰, or by Kusunose and Harima⁹.

The present analysis allows us to qualitatively compare the measured normalized elastic constants [Figs. 3 (a), (b), and (c)] with the calculated quadrupolar susceptibilities as shown in Figs. 3 (d), (e), and (f) (Appendix A). At first glance, none of these CEF schemes successfully reproduces experimental observations. A detailed analysis follows below;

(i) $(C_{11} - C_{12})/2$, $\Gamma_3(B_{1g})$ symmetry:

Only the Scheme 1 and Scheme 3 reproduce the temperature and magnetic field dependence of $(C_{11} - C_{12})/2$. Scheme 2 shows a steep softening below 20 K at $H = 0$ T and Scheme 4 shows a broad minimum at around 50 K at $H = 0$ and 60 T, inconsistent with the experimental data at low and high magnetic fields.

(ii) C_{66} , $\Gamma_4(B_{2g})$ symmetry:

TABLE II. Labels, CEF level scheme, active multipoles, author and references

Labels	Level Scheme (K)	Active Multipoles (Symmetry)	Authors Ref.
Scheme 1	$\Gamma_1^{(1)} - \Gamma_2(60) - \Gamma_3(178) - \Gamma_5^{(1)}(491) - \dots$	$H_z^\alpha (A_{2g})$	Yanagisawa <i>et al.</i> [28]
Scheme 2	$\Gamma_5^{(1)} - \Gamma_1^{(1)}(404) - \Gamma_2(1076) - \dots$	$O_2^2(B_{1g})$	Ohkawa and Shimizu, Galatanu <i>et al.</i> [29]
Scheme 3	$\Gamma_3 - \Gamma_1^{(1)}(44) - \Gamma_2(112) - \Gamma_5^{(1)}(485) \dots$	$O_2^2(B_{1g})$ or $T_{xyz}(B_{1u})$	Santini and Amoretti [30]
Scheme 4	$\Gamma_1^{(1)} - \Gamma_5^{(2)}(140) - \Gamma_2(300) \dots$	$T_x^\beta(E_u)$	Hanzawa and Watanabe [31]

Only Scheme 3 roughly reproduces the temperature dependence of C_{66} at high magnetic field. However, the expected softening at 0 T in Scheme 3 is not seen in the experimental data. Scheme 2 again shows a steep softening at $H = 0$ below 20 K and Scheme 1 and Scheme 4 show local minima and upturns; inconsistent with the experiment.

(iii) C_{44} , $\Gamma_5(E_g)$ symmetry:

Only Scheme 4 reproduces the softening at 60 T, but its magnetic-field dependence shows an opposite tendency (no softening in magnetic field). All the other schemes (1-3) show neither low-temperature softening nor enhancement under magnetic fields.

Therefore, based on this logic, we conclude that the present experimental results can not be fully explained by CEF schemes in the $5f^2$ configuration. Note that other CEF schemes have been tested and also resulted in poor agreement with the experimental data. For example, $\Gamma_1^{(1)} - \Gamma_4(45 \text{ K}) - \Gamma_5^{(2)}(51 \text{ K}) - \Gamma_2(100 \text{ K})$ [32], which cannot be explained by tetragonal CEF since this theory is considering many-body effects, $\Gamma_1^{(1)} - \Gamma_2(42 \text{ K}) - \Gamma_1^{(2)}(170 \text{ K})$ [27], and $\Gamma_4 - \Gamma_1^{(1)}(44 \text{ K}) - \Gamma_2(112)$ [30].

Here, we discuss conditions for the application of the CEF schemes to URu_2Si_2 . As mentioned, the $5f^2$ non-Kramers multiplet is the best assumption to reproduce the anisotropy in the magnetization. Because J_z has diagonal matrix elements in doublet states and off-diagonal elements between singlet-singlet, doublet-doublet, while J_x and J_y only have off-diagonal elements between singlet-doublet. Thus, if the singlet and doublet states are separated in non-Kramers $J = 4$ CEF states (like Schemes 1 and 2), one can naturally get magnetic anisotropy. Indeed, CEF Schemes 3 and 4, where the singlet and doublet are relatively close ($\leq 300 \text{ K}$), cannot fully reproduce the anisotropic magnetization.

On the other hand, all CEF schemes above are inconsistent with the occurrence of the softening in C_{44} mode, because the corresponding quadrupolar moments of O_{yz} and O_{zx} , which has $\Delta J = \pm 1$ transition and always accompany with magnetic moment J_z . Thus, it is difficult to find a CEF scheme which satisfies the mutually exclusive features. Therefore, it is even more challenging to find a CEF scheme which balances the competing transitions of O_{xy} with $\Delta J = \pm 2$, and O_{yz} and O_{zx} with $\Delta J = \pm 1$ and also reproduces all elastic constant softenings at high magnetic fields, where the present system is

not affected by both c - f hybridization and PPM states. Therefore, we need to find an appropriate CEF scheme and/or consider another origin or modulation to reproduce the experimental data.

One possibility is a rotation effect^{33,34}. A rotation invariant of the Hamiltonian describing quadrupole-strain interaction will produce a finite modulation of the transverse mode under magnetic field. In the present experiments, the geometry of the C_{44} mode ($k \parallel [100]$, $u \parallel H \parallel [001]$) is the case to consider this effect. This ultrasonic mode induces the strain field ϵ_{zx} and also induces the rotation of ω_{zx} , which will couple to the magnetic torque of the total angular momentum J . We tried to compute such an effect on CEF Scheme 3 which originally show no softening in C_{44} , but the rotation does not reproduce this. CEF Scheme 1, on the other hand, can generate the softening in C_{44} when the rotation effect is considered (not shown). To verify whether this modulation exists or not, further measurements of C_{44} with different geometries, for example ($k \parallel H \parallel [001]$, $u \parallel [100]$) and ($k \parallel H \parallel [100]$, $u \parallel [001]$), need to be performed.

C. Consideration of Hexadecapolar Contribution

In contrast to C_{44} and other modes, C_{66} measured with ($k \parallel [100]$, $u \parallel [010]$, and $H \parallel [001]$), has no rotation-effect contribution. As mentioned, none of these CEF schemes could reproduce the low-temperature softening of C_{66} in high magnetic field.

A possible explanation for this softening is a higher-rank multipolar contribution, such as an electric hexadecapolar contribution to the elastic constant. As shown in Table I, the transverse ultrasonic mode C_{66} and $(C_{11} - C_{12})/2$, which propagate in the c plane ($k \perp [001]$) also induce the rotation ω_{xy} , which couples to the electric hexadecapole $H_z^\alpha = \sqrt{35}(J_+^4 - J_-^4)/4i$, with $\Gamma_2(A_{2g})$ symmetry (Appendix B). This is the theoretically predicted order parameter of Scheme 1 in Table II. It should also be noted that recent inelastic x-ray scattering measurements showed that the $5f$ ground-state wave function is composed mainly of Γ_1 and/or Γ_2 , which is consistent with CEF Scheme 1.³⁵

Additionally, from recent resonant x-ray scattering measurements, no superlattice reflections or azimuthal angle-dependences which evidence rank 2 and 3 multipolar order have been observed so far³⁶. Thus, the lower-rank electric quadrupole order and magnetic octupolar

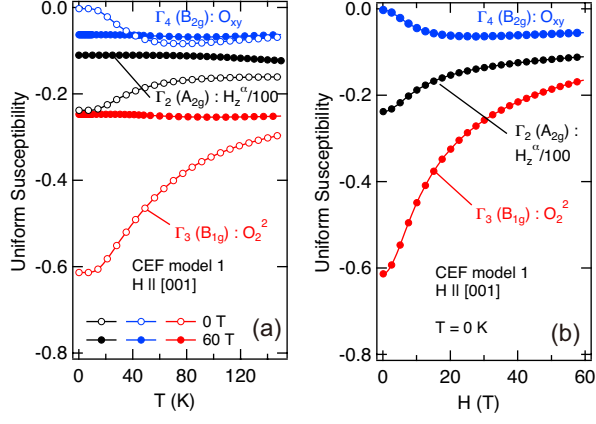


FIG. 5. Calculated uniform multipolar susceptibilities including the $\Gamma_3(B_{1g})$ and the $\Gamma_4(B_{2g})$ -Quadrupole terms O_2^2 and O_{xy} , respectively, and the $\Gamma_2(A_{2g})$ -Hexadecapole term H_z^α by using CEF model 1 (see Table II) (a) temperature dependence at 0 T (open symbol) and 60 T (closed symbol) and (b) magnetic field dependence at 0 K.

order can be eliminated as candidates for the HO parameter. The remaining unsubscribed order is an electric hexadecapole order with A_{2g} symmetry or a composite order corresponding to this symmetry such as the chiral density wave order with $A_{2g} \pm B_{1g}$ symmetry.³⁷ Since the elastic response of chiral density waves are not fully understood, the following analysis is based on the H_z^α -type hexadecapolar order predicted by Kusunose *et al.*⁹ with CEF Scheme 1, where the H_z^α moment is active. Figure 5 show the uniform hexadecapolar susceptibility and quadrupole susceptibility as a function of temperature (Fig. 5(a)) and magnetic field (Fig. 5(b)) calculated by using CEF Scheme 1. The susceptibility of $H_z^\alpha(A_{2g})$ shows the opposite temperature dependence as compared to $O_{xy}(B_{2g})$ and similar temperature dependence as $O_2^2(B_{1g})$ with a relatively larger matrix element (H_z^α in Figs. 5 are divided by 100). Again, the response shows the opposite tendency to the increasing of the softening in higher-magnetic field regions. Since the rotation of ω_{xy} is unitary transformation, the hexadecapole moment will not affect the single-ion Hamiltonian at zero magnetic field and/or under the field applied along z ([001]) axis. In other words, this hexadecapole will affect the sound velocity only when a finite magnetic field along xy plane and/or anisotropic multipolar interaction exist. Thus, we need to assume a large anisotropy in the coupling mechanism of hexadecapolar-lattice interactions and a two-electron Hamiltonian to reproduce the opposite elastic responses between the C_{66} and $(C_{11} - C_{12})/2$. A similar elastic response and characteristic ultrasonic attenuation were observed in C_{66} mode of the iron-based superconductor $\text{Ba}(\text{Fe}_{1-x}\text{Co}_x)_2\text{As}_2$ ($x = 0.1$)³⁸, where a hexadecapolar order and its instability towards the superconducting phase was predicted. However, the authors mention that the hexadecapolar contribution is estimated to be 250 times smaller than the quadrupolar

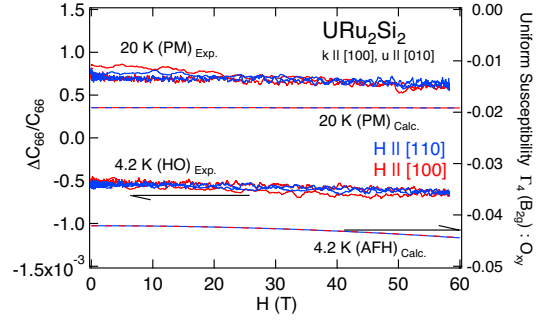


FIG. 6. (Left axis): Magnetic field dependence of elastic constant C_{66} for $H \parallel [100]$ and $H \parallel [110]$ of URu_2Si_2 at 4.2 K and 20 K. (Right axis): Calculated (uniform) quadrupolar susceptibility using the mean-field theory with CEF Scheme 1 as described in the text.

contribution in this iron-based superconductor. Therefore, the hexadecapolar contribution of the present elastic constants $(C_{11} - C_{12})/2$ and C_{66} for URu_2Si_2 is also expected to be miniscule, and will not reproduce the softening of C_{66} in high magnetic fields, unless the hexadecapolar contribution is strongly enhanced for some unknown reason.

Using a different approach, we also checked the hexadecapolar contribution on the elastic constant C_{66} in a magnetic field applied perpendicular to c axis. Figure 6 shows the magnetic-field dependence of the elastic constant C_{66} for $H \parallel [100]$ and $H \parallel [110]$ of URu_2Si_2 at 4.2 and 20 K. There is no obvious difference of the data below and above T_O and for both field orientations within the present measurement accuracy. The quadrupolar susceptibility was calculated using a mean-field approximation, which assumes the H_z^α -type antiferro-hexadecapolar interaction as the HO parameter, based on the theory of Kusunose *et al.*⁹, which predicts that a very tiny difference should appear between the [100] and [110] directions in the antiferro-hexadecapole (AFH) order state. The calculated uniform quadrupolar susceptibility using the mean field theory²⁸ with CEF model 1 is also displayed in Fig. 5. This predicted anisotropy between $H \parallel [100]$ (red line) and $H \parallel [110]$ (blue line) can not be distinguished in the present scale of Fig. 6. We have reported similar results for the mode $(C_{11} - C_{12})/2$ in the previous paper [28]. Thus, as in the previous investigation, higher magnetic fields and/or improved measurement accuracy, such as using static magnetic fields, are required to ultimately rule out the existence of hexadecapole interaction. In conclusion, a hexadecapolar order is not indicated within the present measurement accuracy under pulsed magnetic field. The origin of the enhanced softening of C_{66} for $H \parallel [001]$ at high magnetic fields remains an open question.

D. Comments on the Low possibility of Rotational Symmetry Breaking in the HO

Finally, we comment on the recently proposed symmetry-breaking scenarios. Tonegawa *et al.* reported that the lattice symmetry is broken from tetragonal to orthorhombic only when using a sample with very high RRR as found in synchrotron x-ray measurements⁶. Ultrasound is a highly powerful tool to detect symmetry-breaking lattice distortions even when the lattice distortions are staggered or small. For example, the tetragonal systems DyB_2C_2 ³⁹ and BaFe_2As_2 ^{38,40} systems show a ϵ_{xy} -type staggered/uniform lattice distortion due to antiferro-/ferro-quadrupolar order. A clear softening towards the phase transitions was observed in the related symmetric ultrasonic modes. The absence of such softening in C_{66} leaves a ϵ_{xy} -type orthorhombic lattice distortion in the HO highly unlikely. Namely, there will be no tetragonal to orthorhombic (4- to 2-fold) symmetry breaking in the HO. Instead, the softening is enhanced above 37 T where the hidden order is suppressed. It should be noted that C_{66} shows a relatively large jump at T_O in the temperature dependence at 30 T for $H \parallel [001]$ [as indicated by the red arrowhead in Fig. 3(b)]. This fact may suggest the freezing of the related multipolar degrees of freedom O_{xy} or H_z^α at T_O . However, these features appear already above the region of the Fermi-surface reconstruction, which has been pointed out by Shishido *et al.* based on the Hall-effect measurement⁴¹. Thus, it is not clear whether the enhancement of the elastic anomaly of C_{66} at T_O in magnetic field is related to the origin of pure HO parameter. To more precisely determine the response of C_{66} in these magnetic field regions, further investigation, such as ultrasonic measurements under static magnetic field around 30 T, are needed.

V. SUMMARY

We performed ultrasonic measurements on URu_2Si_2 in pulsed magnetic fields to check the elastic responses of this compound and found that the $\Gamma_3(\text{B}_{1g})$ -type lattice instability is dominant at low temperature and low magnetic fields. In contrast, we observed enhancements of the elastic softening of the $\Gamma_4(\text{B}_{2g})$ and $\Gamma_5(\text{E}_g)$ symmetric modes towards low temperatures at magnetic fields above 40 T. We discussed the origin of these elastic responses based upon the D_{4h} symmetry point group analysis, starting from a local multipolar state (crystalline electric field) assuming weak hybridization and used an itinerant scheme based on the deformation-potential coupling due to the band-Jahn-Teller effect of a strongly c - f hybridized band which becomes weaker as the field is increased. The present analysis revealed again that the itinerant-band Jahn-Teller model is more applicable and the c - f hybridization is important in HO. On the other hand, the results cannot be explained by the quadrupolar susceptibility based on the crystalline-electric-field

schemes in the $5f^2$ -configuration which have been proposed thus far. To conclude, this work revealed important information on the elastic response towards the crossover from the delocalized to the localized electric state of the present system. However, a comprehensive interpretation of these elastic responses is still pending, and further investigations will be required.

ACKNOWLEDGMENTS

The present research was supported by JSPS KAKENHI Grant Numbers JP17K05525(C), JP16H04006, JP15H05882, JP15H05884, JP15H05745, JP15KK0146, JP15K21732, JP23740250 and JP23102701 and the Strategic Young Researcher Overseas Visits Program for Accelerating Brain Circulation from JSPS. Experiments performed in the United States were supported by US DOE, Grant Number DE-FG02-04-ER46105. Experiments performed at CEA Grenoble were supported by the ERC Starting Grant (NewHeavyFermion), and ANR (SINUS). One of the authors T.Y. would like to thank Prof. John A. Mydosh, Prof. Hiroaki Kusunose, Dr. Trevor Keiber, and Mr. Dave Landry for fruitful discussions. We also acknowledge the support of the Hochfeld-Magnetlabor Dresden at HZDR, a member of the European Magnetic Field Laboratory.

Appendix A: Formulation of the Multipolar Susceptibility

We start from the CEF Hamiltonian with elastic-strain mediated perturbation,

$$\mathcal{H} = \mathcal{H}_{\text{CEF}} + \sum_{\epsilon_\Gamma} \frac{\partial \mathcal{H}_{\text{CEF}}}{\partial \epsilon_\Gamma} \epsilon_\Gamma. \quad (\text{A1})$$

The tetragonal CEF Hamiltonian with Zeeman effect is written as

$$\begin{aligned} \mathcal{H}_{\text{CEF}} = & B_2^0 O_2^0 + B_4^0 O_4^0 + B_4^4 O_4^4 + B_6^0 O_6^0 + B_6^4 O_6^4 \\ & + gJ\mu_B \sum_{i=x,y,z} J_i H_i. \end{aligned} \quad (\text{A2})$$

Here, B_m^n are the CEF parameters and O_m^n are the Stevens operators. The numerical values of B_m^n , which were used in the present analysis, are listed in Table III.

The second term of Eq. (A1) is explained in terms of electric multipole-strain interaction. Especially for rank-2 multipoles (quadrupoles), this term is written as

$$\mathcal{H}_{\text{MS}}^{(2)} = -g_{\Gamma_3}^{(2)} O_2^0 \epsilon_v - g_{\Gamma_4}^{(2)} O_{xy} \epsilon_{xy} - g_{\Gamma_5}^{(2)} \{O_{yz} \epsilon_{yz} + O_{zx} \epsilon_{zx}\}. \quad (\text{A3})$$

For rank-4 multipoles (hexadecapoles), we assume a bilinear coupling between hexadecapoles and rotations with the same $\Gamma_2(\text{A}_{2g})$ symmetry instead of using a symmetrized strain ϵ_Γ as a perturbation field,

$$\mathcal{H}_{\text{MS}}^{(4)} = -g_{\Gamma_2}^{(4)} H_z^\alpha \omega_{xy}. \quad (\text{A4})$$

TABLE III. CEF parameters for the present analysis

Labels	Level Scheme (K)	B_2^0 (K)	B_4^0 (K)	B_4^4 (K)	B_6^0 (K)	B_6^4 (K)
Scheme 1	$\Gamma_1^{(1)} - \Gamma_2(60) - \Gamma_3(178) - \Gamma_5^{(1)}(491) - \dots$	12.0	-0.43	-3.2	-0.011	0.053
Scheme 2	$\Gamma_5^{(1)} - \Gamma_1^{(1)}(404) - \Gamma_2(1076) - \dots$	-26.0	-0.01	0.3	0.062	-0.05
Scheme 3	$\Gamma_3 - \Gamma_1^{(1)}(44) - \Gamma_2(112) - \Gamma_5^{(1)}(485) - \dots$	-7.6241	-0.09658	-0.49981	-0.01165	0.07022
Scheme 4	$\Gamma_1^{(1)} - \Gamma_5^{(2)}(140) - \Gamma_2(300) - \dots$	-7.3985	-0.01727	1.11324	0.00890	-0.11656

Here, $g_\Gamma^{(2)}$ and $g_\Gamma^{(4)}$ are the coupling constants for the rank-2 and rank-4 multipoles, respectively. O_Γ and H_Γ^α are quadrupole and hexadecapole operators, respectively. Those are listed in Table I and the quadrupole operators are also defined in Appendix B. The free energy of the local $5f$ electronic states in the CEF can be written as

$$F = U = Nk_B T \ln \sum_n \exp\{-E_n(\epsilon_\Gamma)/k_B T\}. \quad (\text{A5})$$

Here, N is the number of ions in a unit volume, $E_n(\epsilon_\Gamma)$ is a perturbed CEF level as a function of strain ϵ_Γ . n is the number index for J multiplets and their degenerate states. U gives the internal energy for the strained system, which is written in terms of the symmetry strains and elastic constants listed in Table I as,

$$U = \frac{1}{2}\{C_B\epsilon_B^2 + C_{Bu}\epsilon_B\epsilon_u + C_u\epsilon_u^2 + C_v\epsilon_v^2 + C_{44}(\epsilon_{yz}^2 + \epsilon_{zx}^2) + C_{66}\epsilon_{xy}^2\}. \quad (\text{A6})$$

Here, $C = -(C_{11}^0 + C_{12}^0 - C_{13}^0 - C_{14}^0)/\sqrt{3}$. In second perturbation, the temperature dependence of the elastic constant is given by

$$C_\Gamma(T, H) = C_\Gamma^0 - N(g_\Gamma^{(2)})^2 \chi_\Gamma(T, H). \quad (\text{A7})$$

Here, C_Γ^0 is the background of the elastic constant. The single-ion multipolar susceptibility χ_Γ is defined as the second derivative of the free energy with respect to strain (in the $\epsilon_\Gamma \rightarrow 0$ limit),

$$-(g_\Gamma^{(2)})^2 \chi_\Gamma = -\left\langle \frac{\partial^2 E_n}{\partial \epsilon_\Gamma^2} \right\rangle + \frac{1}{k_{BT}} \left\{ \left\langle \left(\frac{\partial E_n}{\partial \epsilon_\Gamma} \right)^2 \right\rangle - \left\langle \frac{\partial E_n}{\partial \epsilon_\Gamma} \right\rangle^2 \right\}. \quad (\text{A8})$$

Here, the angle brackets mean the thermal average. Note that, when we use the rotation ω_{xy} as a conjugate field for the hexadecapole moment, we need to assume some mechanism of the anisotropic hexadecapolar interaction, *e.g.*, a two electron state, as discussed in Ref. 38, because the rotation ω_{xy} is a unitary transformation for the system, *i.e.*, it does not change the single-ion Hamiltonian at zero magnetic field. If Eq. (A4) is valid, we can substitute ω_{xy} for ϵ_{xy} in the formulas above to determine the hexadecapolar susceptibility. Eq. (A6) can be rewritten

in the form of a normalized elastic constant as shown in Fig. 3 (a), (b), and (c).

$$\Delta(C_\Gamma(T, H) - C_\Gamma^0) = \left[\frac{C_\Gamma(T, H) - C_\Gamma^0(T)}{C_{\Gamma(T=1.5K)}^0} \right] = \frac{N(g_\Gamma^{(2)})^2}{C_{\Gamma(T=1.5K)}^0} \chi_\Gamma(T, H). \quad (\text{A9})$$

In the present analysis, we assume $C_\Gamma^0(T) = C_{ph}(T)$ as the phonon contribution, which is obtained from the elastic constant of ThRu₂Si₂ without $5f$ -electron contribution. We now have the tools to compare the temperature- and magnetic-field dependence of the normalized elastic constants with the quadrupole susceptibility by assuming $A = N(g_\Gamma^{(2)})^2/C_{\Gamma(T=1.5K)}^0$ being independent from T and H .

Appendix B: Definition of Multipolar Moments and Equivalent Operator Expression

The electric multipolar operators are defined by multipolar expansion of the electrostatic potential as,

$$Q_{lm} \equiv e \sum_{j=1}^{n_f} r_j^l Z_{lm}^*(r_j). \quad (\text{B1})$$

Here, $e < 0$ is the electron charge, n_f is the number of f electrons. $Z_{lm}(r_j)$ is written by using spherical harmonics $Y_{lm}(r_j)$ as,

$$Z_{lm}(r_j) \equiv \sqrt{4\pi/(2l+2)} Y_{lm}^*(r_j). \quad (\text{B2})$$

Eq.(B1) can be rewritten by replacing (x, y, z) in Z_{lm} with spherical tensor operators J_{lm} with following transformations,

$$x^{n_x} y^{n_y} z^{n_z} \rightarrow \frac{n_x! n_y! n_z!}{(n_x + n_y + n_z)!} \sum_{\mathcal{P}} \mathcal{P}(J_x^{n_x} J_y^{n_y} J_z^{n_z}). \quad (\text{B3})$$

Here, \mathcal{P} is a sum of all possible permutations. Operator J_{lm} has the following commutation relation, with the ladder operator $J_\pm = J_x \pm iJ_y$:

$$J_{ll} = (-1)^l \sqrt{\frac{(2l-1)!!}{(2l)!}} (J_+)^l, \quad (\text{B4})$$

$$[J_-, J_{lm}] = \sqrt{(l+m)(l-m+1)} J_{lm-1}. \quad (\text{B5})$$

Following are quadrupolar and hexadecapolar operators, which are used in the present analysis:

i) Rank 2 (Quadrupole)

$\Gamma_3(B_{1g}) :$

$$O_2^2 = O_v = \frac{i}{\sqrt{2}} [J_{22} + J_{2-2}] = \frac{\sqrt{3}}{2} (J_x^2 - J_y^2) \quad (\text{B6})$$

$\Gamma_4(B_{2g}) :$

$$O_{xy} = \frac{i}{\sqrt{2}} [-J_{22} + J_{2-2}] = \frac{\sqrt{3}}{2} (J_x J_y - J_y J_x) \quad (\text{B7})$$

$\Gamma_5(E_g) :$

$$O_{yz} = \frac{i}{\sqrt{2}} [J_{21} + J_{2-1}] = \frac{\sqrt{3}}{2} (J_y J_z - J_z J_y) \quad (\text{B8})$$

$\Gamma_5(E_g) :$

$$O_{zx} = \frac{i}{\sqrt{2}} [-J_{21} + J_{2-1}] = \frac{\sqrt{3}}{2} (J_z J_x - J_x J_z) \quad (\text{B9})$$

ii) Rank 4 (Hexadecapole)

$\Gamma_2(A_{2g}) :$

$$\begin{aligned} H_z^\alpha &= \frac{\sqrt{35}}{4i} [-J_{44} + J_{4-4}] \\ &= \frac{\sqrt{35}}{8} \{ (J_x^3 J_y + J_x^2 J_y J_x + J_x J_y J_x^2 + J_y J_x^3) \\ &\quad - (J_x J_y^3 + J_y^2 J_x J_y + J_y J_x J_y^2 + J_x J_y^3) \} \quad (\text{B10}) \end{aligned}$$

* tatsuya@phys.sci.hokudai.ac.jp

- ¹ T. T. M. Palstra, A.A.Menovsky, J. den Berg, A. J. Dirkmaat, P. H. Kes, G. J. Nieuwenhuys, and J. A. Mydosh, Phys. Rev. Lett. **55**, 2727 (1985).
- ² M. B. Maple, J. W. Chen, Y. Dalichaouch, T. Kohara, C. Rossel, M. S. Torikachvili, M. W. McElfresh, and J. D. Thompson, Phys. Rev. Lett. **56**, 185 (1986).
- ³ W. Schlitz, J. Baumann, B. Pollit, U. Rauchschwalbe, H. M. Mayer, U. Ahlheim, and C. D. Bredl, Z. Phys. B **62**, 171 (1986).
- ⁴ J. A. Mydosh and P. M. Oppeneer, Rev. Mod. Phys. **83**, 1301 (2011).
- ⁵ R. Okazaki, T. Shibauchi, H. J. Shi, Y. Haga, T. D. Matsuda, E. Yamamoto, Y. Ōnuki, H. Ikeda, and Y. Matsuda, Science **331**, 439 (2011).
- ⁶ S. Tonegawa, S. Kasahara, T. Fukuda, K. Sugimoto, N. Yasuda, Y. Tsuruhara, D. Watanabe, Y. Mizukami, Y. Haga, T. D. Matsuda, E. Yamamoto, Y. Ōnuki, H. Ikeda, Y. Matsuda, and T. Shibauchi, Nature Comm. **5**, 4188 (2014).
- ⁷ J. Buhot, M. A. Méasson, Y. Gallais, M. Cazayous, A. Sacuto, G. Lapertot, and D. Aoki, Phys. Rev. Lett. **113**, 266405 (2014).
- ⁸ S. C. Riggs, M. C. Shapiro, A. V. Maharaj, S. Raghu, E. D. Bauer, R. E. Baumbach, M. W. P. Giraldo-Gallo, and I. R. Fisher, Nature Comm. **6**, 6425 (2015).
- ⁹ H. Kusunose and H. Harima, J. Phys. Soc. Jpn. **80**, 084702 (2011).
- ¹⁰ K. Haule and G. Kotliar, Nature Phys. **5**, 796 (2009).
- ¹¹ H. Ikeda, M. T. Suzuki, R. Arita, T. Takimoto, T. Shibauchi, and Y. Matsuda, Nature Phys. **8**, 528 (2012).
- ¹² E. Ressouche, R. Ballou, F. Bourdarot, D. Aoki, V. Simonet, M. T. Fernandez-Diaz, A. Stunault, and J. Flouquet, Phys. Rev. Lett. **109**, 067202 (2012).
- ¹³ J. G. Rau and H. Y. Kee, Phys. Rev. B **85**, 245112 (2012).
- ¹⁴ P. Chandra, P. Coleman, J. A. Mydosh, and V. Tripathi, Nature **417**, 831 (2002).
- ¹⁵ P. S. Riseborough, B. Coqblin, and S. G. Magalhães, Phys. Rev. B **85**, 165116 (2012).

- ¹⁶ S. Elgazzar, J. Ruzs, M. Amft, P. M. Oppeneer, and J. A. Mydosh, Nature Mat. **8**, 337 (2009).
- ¹⁷ K. H. Kim, N. Harrison, M. Jaime, G. S. Boebinger, and J. A. Mydosh, Phys. Rev. Lett. **91**, 256401 (2003).
- ¹⁸ G. W. Scheerer, W. Knafo, D. Aoki, G. Ballon, A. Mari, D. Vignolles, and J. Flouquet, Phys. Rev. B **85**, 094402 (2012).
- ¹⁹ W. Knafo, F. Duc, F. Bourdarot, K. Kuwahara, H. Nojiri, D. Aoki, J. Billette, P. Frings, X. Tonon, E. Lelievre-Berna, J. Flouquet, and L.-P. Regnault, Nature Comm. **7**, 13075 (2016).
- ²⁰ T. Yanagisawa, S. Mombetsu, H. Hidaka, H. Amitsuka, M. Akatsu, S. Yasin, S. Zherlitsyn, J. Wosnitza, K. Huang, M. Janoschek, and M. B. Maple, Phys. Rev. B **88**, 195150 (2013).
- ²¹ The present geometry of C_{33} ($k \parallel u \parallel H$ [001]) has the largest cross section of our transducers, which have gold evaporated electric terminals. There could be a small change of the sample temperatures due to eddy current heating of the transducers perpendicular to the applied magnetic field. Hence, the elastic anomaly appearing in C_{33} deviates from the expected phase boundaries position due to the additional heating during the pulse. Such eddy-current heating is not an issue for other ultrasonic modes, where the transducers have a smaller cross section.
- ²² V. F. Correa, S. Francoual, M. Jaime, N. Harrison, T. P. Murphy, E. C. Palm, S. W. Tozer, A. H. Lacerda, P. A. Sharma, and J. A. Mydosh, Phys. Rev. Lett. **109**, 246405 (2012).
- ²³ W. Knafo, C. Meingast, K. Grube, S. Drobnik, P. Popovich, P. Schweiss, P. Adelman, T. Wolf, and H. v. Löhneysen, Phys. Rev. Lett. **99**, 137206 (2007).
- ²⁴ T. Yanagisawa, H. Saito, Y. Watanabe, Y. Shimizu, H. Hidaka, and H. Amitsuka, J. Phys. Conf. Ser. **391**, 012079 (2012).
- ²⁵ B. Lüthi, *Physical Acoustics in the Solid State* (Springer, 2006).
- ²⁶ K. Knorr, B. Renker, W. Assmus, B. Lüthi, R. Takke, and H. J. Lauter, Z. Phys. B **39**, 151 (1980).

- ²⁷ G. J. Nieuwenhuys, Phys. Rev. B **35**, 5260 (1987).
- ²⁸ T. Yanagisawa, S. Mombetsu, H. Hidaka, H. Amitsuka, M. Akatsu, S. Yasin, S. Zherlitsyn, J. Wosnitza, K. Huang, , and M. B. Maple, J. Phys. Soc. Jpn. **82**, 013601 (2011).
- ²⁹ A. Galatanu, Y. Haga, T. D. Matsuda, S. Ikeda, E. Yamamoto, D. Aoki, T. Takeuchi, and Y. Ōnuki, J. Phys. Soc. Jpn. **74**, 1582 (2005).
- ³⁰ P. Santini and G. Amoretti, Phys. Rev. Lett. **73**, 1027 (1994).
- ³¹ K. Hanzawa and N. Watanabe, J. Phys.: Condens. Matter **17**, L419 (2005).
- ³² A. Kiss and P. Fazekas, Phys. Rev. B **71**, 054415 (2005).
- ³³ V. Dohm and P. Fulde, Z. Phys. B **21**, 369 (1975).
- ³⁴ P. Thalmeier and P. Fulde, Z. Phys. B **22**, 359 (1975).
- ³⁵ M. Sundermann, M. W. Haverkort, S. Agrestini, A. Al-Zein, M. M. Sala, Y. Huang, M. Golden, A. de Visser, P. Thalmeier, L. H. Tjeng, and A. Severing, Proc. Natl. Acad. Sci. **113**, 13989 (2016).
- ³⁶ H. Amitsuka, T. Inami, M. Yokoyama, S. Takayama, Y. Ikeda, I. Kawasaki, Y. Homma, H. Hidaka, and T. Yanagisawa, J. Phys.: Conf. Series **200**, 012007 (2010).
- ³⁷ H.-H. Kung, R. E. Baumbach, E. D. Bauer, V. K. Thorsmolle, W.-L. Zhang, K. Haule, J. A. Mydosh, and G. Blumberg, Science **347**, 1339 (2015).
- ³⁸ R. Kurihara, K. Mitsumoto, M. Akatsu, Y. Nemoto, T. Goto, Y. Kobayashi, and M. Sato, J. Phys. Soc. Jpn. **86**, 064706 (2017).
- ³⁹ Y. Nemoto, T. Yanagisawa, K. Hyodo, T. Goto, S. Miyata, R. Watanuki, and K. Suzuki, Physica B **329-333**, 641 (2003).
- ⁴⁰ M. Yoshizawa, D. Kimura, T. Chiba, S. Simayi, Y. Nakanishi, K. Kihou, C. H. Lee, A. Iyo, H. Eisaki, M. Nakajima, and S. Uchida, J. Phys. Soc. Jpn. **81**, 024604 (2012).
- ⁴¹ H. Shishido, K. Hashimoto, T. Shibauchi, T. Sasaki, H. Oizumi, N. Kobayashi, T. Takamasu, K. Takehana, Y. Imanaka, T. D. Matsuda, Y. Haga, Y. Ōnuki, and Y. Matsuda, Phys. Rev. Lett. **102**, 156403 (2009).